Proximate Tomonaga-Luttinger liquid in a spin-1/2 ferromagnetic XXZ chain compound

Boqiang Li,* Xun Chen,* Yuqian Zhao,* Zhaohua Ma, Zongtang Wan, and Yuesheng Li†
Wuhan National High Magnetic Field Center and School of Physics, Huazhong University of Science and Technology, 430074 Wuhan, China

(Received 23 February 2024; revised 19 May 2024; accepted 9 July 2024; published 23 July 2024)

The spin-1/2 ferromagnetic XXZ chain is a prototypical many-body quantum model, exactly solvable via the integrable Bethe ansatz method, hosting a Tomonaga-Luttinger spin liquid. However, its clear experimental realizations remain absent. Here, we present a thorough investigation of the magnetism of the structurally disorder-free compound $LuCu(OH)_3SO_4$. By conducting magnetization and electron-spin-resonance measurements on the single-crystal sample, we establish that the title compound approximates the spin-1/2 ferromagnetic XXZ chain model with a nearest-neighbor exchange strength of $J_1 \sim 65$ K and an easy-plane anisotropy of $\sim$0.994. The specific heat demonstrates a distinctive power-law behavior at low magnetic fields (with energy scales $\leqslant 0.02J_1$) and low temperatures ($T \leqslant 0.03J_1$). This behavior is consistent with the expectations of the ideal spin-1/2 ferromagnetic XXZ chain model, thereby supporting the formation of a gapless Tomonaga-Luttinger spin liquid in $LuCu(OH)_3SO_4$.

DOI: 10.1103/PhysRevMaterials.8.074410

I. INTRODUCTION

Spin-1/2 many-body correlated systems can give rise to exotic phases and elementary excitations due to their inherent strong quantum fluctuations and entanglements, capturing significant attention in condensed matter physics and materials science. The exploration, understanding, and control of these exotic phases have been a long-standing goal with promising applications in various fields, including future topological quantum computation [1]. However, achieving this task is exceptionally challenging, stemming from two key aspects:

(1) The majority of many-body-correlated quantum systems are too complex to have exact solutions, including eigenstates and eigenvalues. For instance, the ground-state nature of the spin-1/2 kagome-lattice Heisenberg antiferromagnet has been extensively studied for many years but remains elusive [2–5].

(2) Real strongly correlated materials are so complex that their properties cannot be fully captured by simplified theoretical models, particularly in systems with low-lying small-gapped or gapless excitations. The Kitaev model is one of the few exactly solvable spin-1/2 many-body models [6], but its experimental realizations are still under heated debate due to the widespread presence of significant non-Kitaev interactions in real materials [7,8].

The spin-1/2 XXZ or XXX (Heisenberg) chain, originally proposed by Heisenberg and Bethe, is a prototypical many-body model with eigenstates and eigenvalues that can be exactly solved using the integrable Bethe ansatz method [9,10]. In the case of a ferromagnetic nearest-neighbor (NN) exchange interaction (strength J_1) and an easy-plane anisotropy ($0 < \Delta < 1$), the model resides deeply within a gapless Tomonaga-Luttinger spin-liquid phase [11,12]. Numerous candidate compounds for the spin-1/2 ferromagnetic XXZ chain have been previously reported, such as $LiCuVO_4$ [13–17], $LiCuSbO_4$ [18–20], Li_2ZrCuO_4 [21,22], Li_2CuO_2 [23,24], $Ca_2Y_2Cu_5O_{10}$ [25–27], $CuAs_2O_4$ [28], $PbCuSO_4(OH)_2$ [29,30], and others. However, these candidates consistently show substantial next-nearest-neighbor (NNN) antiferromagnetic coupling (J_2), comparable to J_1. Despite their significance as strongly frustrated J_1-J_2 systems, the presence of substantial J_2 typically hinders exact resolution [31]. Furthermore, in the aforementioned Li-based compounds [16,18,21] and $Ca_2Y_2Cu_5O_{10}$ (Ca/Y disorder) [26], structural disorders are inherent and unavoidable. These disorders can introduce significant complications for many-body modeling, given the apparent interaction randomness [32–36].

Recently, Lu *et al.* reported the successful synthesis of the structurally disorder-free Cu^{2+} (spin-1/2) chain compound $LuCu(OH)_3SO_4$, featuring a crystal size of approximately $10 \times 25 \times 10$ μm^3 [37]. However, to the best of our knowledge, its magnetism has not been reported so far. In this study, we implemented a synthesis method and achieved successful growth of significantly larger single crystals of $LuCu(OH)_3SO_4$, typically with a size of $\sim 0.08 \times 1 \times 0.08$ mm^3. Through magnetization and electron-spin-resonance (ESR) measurements on the single-crystal sample, we determined the detailed spin Hamiltonian. Our findings indicate that both interchain and next-nearest-neighbor intrachain couplings are less significant: $J_{p1}/J_1 \sim 1.01\%$, $J_{p2}/J_1 \sim -0.18\%$, and $J_2/J_1 \sim 1\%$ (see Fig. 1). $LuCu(OH)_3SO_4$ closely approximates the ideal spin-1/2 ferromagnetic XXZ chain model with $J_1 \sim 65$ K and $\Delta \sim 0.994$. The specific heat and magnetization measurements down to $T = 35$ mK ($\sim 0.0005J_1$) are consistent with the expectations of the ideal model, supporting the emergence of a gapless Tomonaga-Luttinger spin liquid in $LuCu(OH)_3SO_4$.

*These authors contributed equally to this work.
†Contact author: yuesheng_li@hust.edu.cn

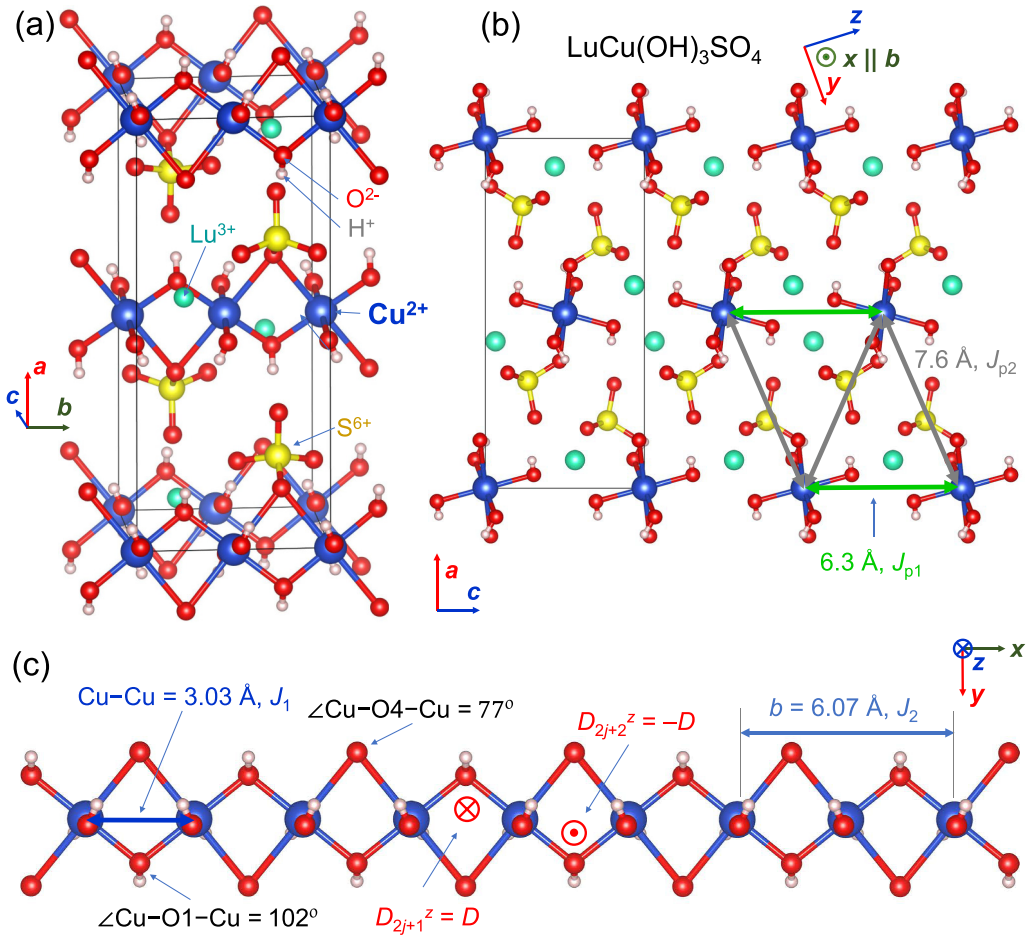

FIG. 1. (a) Crystal structure of $LuCu(OH)_3SO_4$. (b) View along the spin chain (b axis) of the crystal structure. (c) CuO_2 chain viewed along the z axis. Dominant nearest-neighbor (NN) ferromagnetic exchange (J_1) and weaker couplings beyond first neighbors (J_2, J_{p1}, and J_{p2}) are displayed in (b) and (c). NN Dzyaloshinsky-Moriya interaction vectors are shown in (c). The local xyz-coordinate system for spin components is defined, and thin black lines mark the unit cells.

II. METHODS

A. Sample synthesis

The microcrystals of $LuCu(OH)_3SO_4$ were synthesized using the traditional hydrothermal method as reported in Ref. [37], resulting in crystals of approximately $5\times30\times5$ μm^3 in size. To enhance crystal size, we employed copper plates (Cu $\geqslant$ 99.99%) as the Cu source to slow down the chemical reaction. This modification successfully increased the crystal size to $\sim0.08\times1\times0.08$ mm^3 [38]. The high quality and phase purity of our samples were confirmed through both powder and single-crystal x-ray diffraction (XRD) measurements. The longest dimension of the crystal aligns with the b axis, and approximately 800 of the largest single crystals, totaling $\sim$10 mg, are aligned along the b axis using General Electric (GE) varnish for magnetic property measurements. We are only able to align the crystals along the b axis due to the small dimensions that make distinguishing non-b directions challenging.

B. Sample characterizations

The ESR spectra were obtained using a continuous-wave spectrometer (Bruker EMXmicro-6/1) at x-band frequencies ($\sim$9.8 GHz) for both single-crystal and powder samples ($\sim$10 mg). Magnetization and dc/ac susceptibilities of $LuCu(OH)_3SO_4$ (up to 7 T, down to 1.8 K) were measured in a magnetic property measurement system (Quantum Design) using powder samples ($\sim$38 mg, ground from single crystals) and well-aligned single-crystal samples ($\sim$10 mg) along the b axis. The powder sample (6.95 mg) was utilized for magnetization measurements at between 0.035 and 1.8 K, employing a Faraday force magnetometer within a ^{3}He - ^{4}He dilution refrigerator (KELMX-400, Oxford Instruments). Superconducting coils (in INTA-LLD-S12/14, Oxford Instruments) generated the main magnetic fields and field gradients ($dH/dl = \pm10$ T/m), and electrical capacitance was measured using a digital capacitance bridge (AH-2500A, Andeen-Hagerling, Inc.) with the three-terminal method [39,40].

The specific heat measurements, down to 1.8 K, were performed in a Physical Properties Measurement System (Quantum Design) using dry-pressed disks of the powders (4.86 mg). N grease was used to facilitate thermal contact between the power sample and the puck, and the sample coupling was measured to be better than 95%. The specific-heat contributions of the N grease and puck were initially

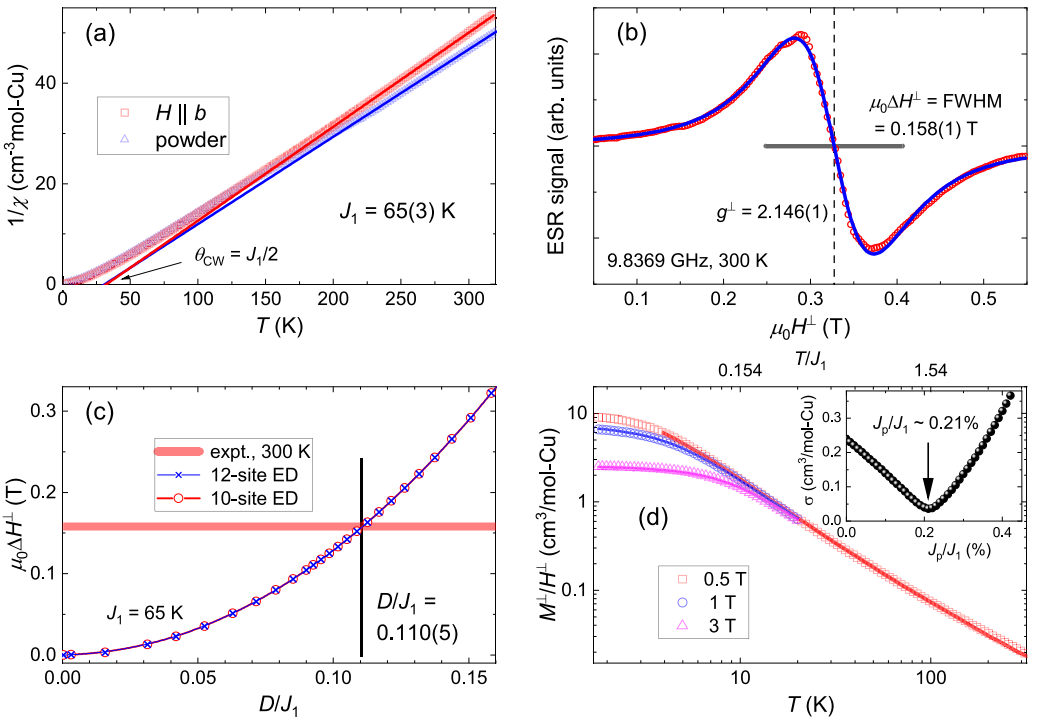

FIG. 2. Determining couplings J_1, D, and $J_p \equiv J_{p1}/3 + 2J_{p2}/3$. (a) Inverse magnetic susceptibilities measured on single-crystal and powder samples, with Curie-Weiss fits (lines) above 200 K. (b) Electron spin resonance (ESR) spectrum measured along the b axis ($H^\perp$) on the single-crystal sample at 300 K. The blue line represents the fit using the derivative Lorentzian function, with resonance field ($g^\perp = 2.146$) and full width at half maximum (FWHM $= \mu_0\Delta H^\perp$) marked. (c) Dzyaloshinsky-Moriya (DM) strength (D) dependence of $\mu_0\Delta H^\perp$, calculated using exact diagonalization (ED) with $J_1 = 65$ K and at $T = 300$ K. The determined DM anisotropic strength is $D/J_1 = 0.110(5)$. (d) Magnetization measured on the single-crystal sample with magnetic fields along the b axis, with stochastic series expansion (SSE) calculations (lines) shown using least-square parameters. Inset: Standard deviation σ as a function of J_p/J_1 calculated using the experimental data between 1.8 and 20 K at $\mu_0 H^\perp = 1$ and 3 T. The arrow denotes the optimal parameter $J_p/J_1 = 0.21(1)\%$. Periodic boundary conditions are used in both ED and SSE computations.

measured and subtracted from the data. Specific heat measurements between 0.1 and 1.8 K were carried out using a thermal relaxation method in the dilution refrigerator, utilizing a powder sample weighing 2.61 mg. The thermal link to the bath was established using a bronze wire of appropriate diameter and length to achieve quasiadiabatic conditions [34,41]. A ~10 nm NiCr layer was deposited on one side of the platform and served as a heater (resistance ~10 kΩ). The chip thermometer (CX-1010-BR, LakeShore) was *in situ* calibrated against a reference thermometer (RX-102B-RS-0.02B, LakeShore, calibrated down to 20 mK) at each applied magnetic field by turning off the heater.

C. Numerical methods

We utilized finite-size ($N \leqslant 28$) exact diagonalization (ED), large-scale ($N = 100$) stochastic series expansion (SSE), and integrable Bethe ansatz ($N \to \infty$) methods to thoroughly investigate the strongly correlated quantum magnetism of $LuCu(OH)_3SO_4$. In the Bethe simulations, we employed $\Delta = \cos(\pi/29)$ (~0.994). Detailed discussions on the validation, consistency, and finite-size effects of these three methods are provided in the Supplemental Material [38].

III. RESULTS AND DISCUSSIONS

A. Crystal structure and symmetry analysis

Figure 1 displays the crystal structure of $LuCu(OH)_3SO_4$ refined using single-crystal XRD data [38]. Due to significant differences among Cu^{2+}, Lu^{3+}, OH^-, and SO_4^{2-}, the occurrence of site-mixing structural disorder is expected to be prohibited. First, our XRD data, measured on both powder and single-crystal samples [38], indeed show no clear evidence of structural disorder, aligning with previously reported results [37]. Second, the single-crystal ESR spectrum, highly sensitive to quasifree magnetic moments induced by structural disorder and interaction randomness [42], does not exhibit any sharp components (linewidth <0.02 T) with hyperfine structures [see Fig. 2(b)]. Last, the single-crystal magnetization can be well reproduced by the *ab initio* model down to ~1.8 K ($\mu_0 H^\perp \geqslant 1$ T) without considering structural disorder [see Fig. 2(d)]. Therefore, we propose $LuCu(OH)_3SO_4$ as a structurally disorder-free compound for the study of strongly correlated quantum magnetism.

The superexchange coupling (J_1) between the NN Cu^{2+} ions, with Cu-Cu distance $b/2 = 3.03$ Å, is mediated by $O1^{2-}$ and $O4^{2-}$ along the spin-1/2 chain, with |Cu-O1| ~ 1.95 Å and ∠Cu-O1-Cu ~102° and |Cu-O4| ~ 2.44 Å and ∠Cu-O4-Cu ~77° (see Fig. 1). When the Cu-O-Cu bond angle exceeds

the critical value of $\varphi_c \sim 96^\circ$, the exchange interaction tends to be antiferromagnetic (AFM). Conversely, a ferromagnetic (FM) exchange interaction is expected when the bond angle is smaller. In $LuCu(OH)_3SO_4$, the superexchanges along the Cu-O1-Cu (AFM) and Cu-O4-Cu (FM) paths may compete. Given that $\varphi_c - \angle$Cu-O4-Cu $\sim 19^\circ$ exceeds $\angle$Cu-O1-Cu $- \varphi_c \sim 6^\circ$, we find the detection of a ferromagnetic nature in J_1 [Fig. 2(a)] within $LuCu(OH)_3SO_4$ to be unsurprising.

Magnetic chains are well spatially separated by nonmagnetic Lu^{3+} and SO_4^{2-} with much larger distances of 6.3 Å along the J_{p1} path and 7.6 Å along the J_{p2} path [see Fig. 1(b)], respectively. This suggests the quasi-one-dimensional nature of the spin system in $LuCu(OH)_3SO_4$. Our density functional theory (DFT) $+U$ calculations for $LuCu(OH)_3SO_4$ semiquantitatively demonstrate that $J_1 \sim 50$ K is ferromagnetic, with $J_{p1}/J_1 \sim 4.8\%$, $J_{p2}/J_1 \sim 0.1\%$, and $J_2/J_1 \sim 1.0\%$ [38]. These results indicate that the spin system of $LuCu(OH)_3SO_4$ closely approximates the ideal spin-1/2 ferromagnetic chain model.

In Cu^{2+}-based magnets, the NN exchange coupling is typically isotropic and symmetric (Heisenberg). In addition to the isotropic NN coupling, the antisymmetric Dzyaloshinsky-Moriya (DM) interaction tends to be dominant, arising from spin-orbit coupling if allowed by symmetry [43,44]. Similar to other Cu^{2+}-based magnets, such as $ZnCu_3(OH)_6Cl_2$ [44] and $YCu_3(OH)_{6.5}Br_{2.5}$ [42], we find, through a standard symmetry analysis, that the nearly Heisenberg Hamiltonian invariant under the *Pnma* space group symmetry of $LuCu(OH)_3SO_4$ [see Fig. 1(c)] is given by

$$\mathcal{H} = -J_1 \sum_j \mathbf{S}_j \cdot \mathbf{S}_{j+1} + D \sum_j (-1)^{j+1} \left(S_j^x S_{j+1}^y - S_j^y S_{j+1}^x\right) + \mathcal{H}', \tag{1}$$

where $\mathcal{H}' = J_2 \sum_j \mathbf{S}_j \cdot \mathbf{S}_{j+2} + J_{p1} \sum_{\langle j,jp1\rangle} \mathbf{S}_j \cdot \mathbf{S}_{jp1} + J_{p2} \sum_{\langle j,jp2\rangle} \mathbf{S}_j \cdot \mathbf{S}_{jp2} + \cdots$ represents interactions beyond the nearest neighbors. The periodic boundary condition, $\mathbf{S}_j \equiv \mathbf{S}_{j+N}$, is considered, where N is an even [45] number of spins (i.e., spin length). Since inversion centers are located at any Cu^{2+} ions, the NNN DM interaction is symmetrically forbidden. The parameter D in Eq. (1) denotes the strength of the NN DM interaction, and its sign does not affect the resulting observables due to symmetry. Therefore, for consistency, we set $D > 0$ throughout this work. Additionally, the superscripts, "$\perp$" and "||", denote the quantity with the applied magnetic field perpendicular and parallel to the z axis of the spin model [see Fig. 1(c)], respectively, throughout this work.

Above $\sim$200 K, the inverse magnetic susceptibilities (χ) of $LuCu(OH)_3SO_4$ exhibit a linear T dependence, following the Curie-Weiss (CW) law, $\chi = C/(T - \theta_{CW})$ [see Fig. 2(a)]. Through CW fits, we obtain the g factor as $g = \sqrt{4k_B C/(\mu_0 N_A \mu_B^2)}$. The resulting values are $g^\perp \sim 2.13$ and $g^{powder} \sim 2.2$, based on magnetic susceptibilities measured on the single-crystal and powder samples, respectively. These values are roughly consistent with the ESR [see Fig. 2(b)] and magnetization data. Additionally, the NN ferromagnetic couplings are fitted to be $J_1 = 2\theta_{CW} = 64.9 \pm 0.7$ and 62.3 ± 0.6 K for the single-crystal and powder samples, respectively [Fig. 2(a)]. Thus, we conclude the ferromagnetic $J_1 = 65(3)$ K for $LuCu(OH)_3SO_4$.

B. Electron spin resonance spectrum

Figure 2(b) displays the x-band ESR spectrum measured on the single-crystal sample of $LuCu(OH)_3SO_4$ with the magnetic field applied along the b axis. The experimental data are well fitted using the first-derivative Lorentzian function [see Fig. 2(b)] [46], revealing a sizable linewidth of $\mu_0 \Delta H^\perp = 0.158(1)$ T. Below, we discuss various sources contributing to the broadening of the ESR signal in the high-T limit.

First, the hyperfine interaction contributes to the ESR linewidth as $\mu_0 \Delta H_h \sim |A_h|^2/(g\mu_B J_1) < 0.01$ mT, where $|A_h| < 500$ MHz is the hyperfine coupling between Cu^{2+} electronic and nuclear spins [47]. Second, the dipole-dipole magnetic interaction also broadens the signal by $\mu_0 \Delta H_d \sim |E_d|^2/(g\mu_B J_1) \sim 0.09$ mT. Here, $|E_d| \sim 2\mu_0 g^2 \mu_B^2/(\pi b^3) \sim 1.9$ GHz represents the strength of the dipole-dipole interaction, and $b/2$ is the NN Cu-Cu distance [see Fig. 1(c)]. Third, as there is only one Wyckoff position for Cu^{2+} ions, the uniform Zeeman interaction cannot broaden the single-crystal ESR signal [44,46,48]. Even when all the above contributions are considered together, they are more than two orders of magnitude smaller than the observed linewidth. Therefore, in the high-T limit ($T \sim 300$ K), the exchange anisotropy of the DM interaction predominantly accounts for the observed ESR linewidth in $LuCu(OH)_3SO_4$, with $\mu_0 \Delta H^\perp \sim D^2/(g\mu_B J_1)$ and $D/J_1 \sim 0.1$, similar to several other Cu^{2+}-based magnets [44].

To determine D precisely, we conduct detailed many-body calculations for the transverse ESR linewidth measured at 300 K using $\mu_0 \Delta H^\perp = \sqrt{2\pi (M_2^x)^3/M_4^x}/(g^\perp \mu_B)$. Here, $M_2^x = \langle [\mathcal{H}_{DM}^x, M^+][M^-, \mathcal{H}_{DM}^x]\rangle / \langle M^+ M^-\rangle$ and $M_4^x = \langle [\mathcal{H}^x, [\mathcal{H}_{DM}^x, M^+]][\mathcal{H}^x, [\mathcal{H}_{DM}^x, M^-]]\rangle / \langle M^+ M^-\rangle$ are the second and fourth moments, respectively [49]. In these expressions, we set $\mathcal{H}_{DM}^x = D \sum_j (-1)^{j+1} (S_j^y S_{j+1}^z - S_j^z S_{j+1}^y)$, $\mathcal{H}^x = -J_1 \sum_j \mathbf{S}_j \cdot \mathbf{S}_{j+1} + \mathcal{H}_{DM}^x - \mu_0 H^\perp g^\perp \sum_j S_j^z$, $M^\pm \equiv \sum_j S_j^x \pm i S_j^y$, and $\langle\, \rangle$ represents the equilibrium thermal average, $\langle O\rangle = \mathrm{Tr}(O e^{-\beta \mathcal{H}^x})/\mathrm{Tr}(e^{-\beta \mathcal{H}^x})$ where $\beta \equiv 1/(k_B T)$. At a high temperature of $T = 300$ K ($\sim 4.6 J_1$), the calculated $\mu_0 \Delta H^\perp$ shows no evident finite-size effect and is a monotone increasing function of D/J_1, as shown in Fig. 2(c). By comparing with the experimental ESR linewidth, we conclude $D/J_1 = 0.110(5)$ for $LuCu(OH)_3SO_4$. Furthermore, the observed g-factor shift from the free electron value $g_e = 2.0023$, $(g^\perp - g_e)/g_e \sim 0.072$ ($\sim D/J_1$) [43], also supports the above conclusion.

In comparison, the main ESR signal of the powder sample is broader, $\mu_0 \Delta H_{powder} \sim 0.36$ T [38]. The ESR linewidth calculated along the z axis is two times larger than the transverse one, $\mu_0 \Delta H^\parallel \sim 2\mu_0 \Delta H^\perp$, which partially accounts for the larger value of $\mu_0 \Delta H_{powder}$. On the other hand, the anisotropy of the g-factor tensor should further explain the observed $\mu_0 \Delta H_{powder}$ in $LuCu(OH)_3SO_4$.

C. Ferromagnetic XXZ chain model

The original spin Hamiltonian of $LuCu(OH)_3SO_4$ [Eq. (1)] includes the NN antisymmetric DM interaction, significantly

increasing the computational cost and making low-T simulations challenging. Therefore, we introduce a unitary transformation operator,

$$\mathcal{T}_u = \exp\left(i\sum_j \phi_j S_j^z\right), \tag{2}$$

where $\phi_j = \arctan(D/J_1)[1-(-1)^{j+1}]/2$. Through a canonical transformation, $\widetilde{\mathcal{H}} = \mathcal{T}_u^\dagger \mathcal{H} \mathcal{T}_u$ [50], we obtain a spin-1/2 ferromagnetic XXZ chain,

$$\widetilde{\mathcal{H}} = -\sqrt{J_1^2+D^2}\sum_j \left(S_j^x S_{j+1}^x + S_j^y S_{j+1}^y + \Delta S_j^z S_{j+1}^z\right) + \mathcal{H}', \tag{3}$$

where $\Delta = J_1/\sqrt{J_1^2+D^2} = 0.994$ shows an easy-plane anisotropy for $LuCu(OH)_3SO_4$. Since the unitary transformation does not change the trace, one can calculate the observable by $\langle O\rangle = \mathrm{Tr}(Oe^{-\beta\mathcal{H}})/\mathrm{Tr}(e^{-\beta\mathcal{H}}) = \mathrm{Tr}(\widetilde{O}e^{-\beta\widetilde{\mathcal{H}}})/\mathrm{Tr}(e^{-\beta\widetilde{\mathcal{H}}})$, where $\widetilde{O} = \mathcal{T}_u^\dagger O \mathcal{T}_u$. We confirmed the equivalence between Eqs. (1) and (3) through finite-size ED calculations.

When a magnetic field is applied along the z axis, the Zeeman term remains invariant under $\mathcal{T}_u$, $\widetilde{\mathcal{H}_Z^\parallel} \equiv \mathcal{H}_Z^\parallel$, and thus we can efficiently utilize the ferromagnetic XXZ chain model expressed in Eq. (3) along with $\mathcal{H}_Z^\parallel$ to calculate observables. In cases where the magnetic field is applied perpendicular to the z axis, such as along the b axis, the Zeeman term is no longer invariant under $\mathcal{T}_u$, leading to expensive computations. Fortunately, for $LuCu(OH)_3SO_4$ with a small tilt angle $\phi_0 = \arctan(D/J_1) \sim 6^\circ$, the differences in observables using $\widetilde{\mathcal{H}}$ [Eq. (3)] plus $\widetilde{\mathcal{H}_Z^\perp}$ (DM, exact) and $\mathcal{H}_Z^\perp$ (XXZ, effective) are negligible within the temperature-field range of our experiments. For magnetization/susceptibility, we find $1 < M_{XXZ}^\perp/M_{DM}^\perp \leqslant 1.003$ ($\sim 1/\cos\phi_0$), which is nearly independent of the chain length N [38]. Similarly, the differences in calculated specific heat $C_{XXZ}^\perp$ and $C_{DM}^\perp$ are also completely negligible, compared to the experimental standard errors. Therefore, below, we utilize $\widetilde{\mathcal{H}}$ [Eq. (3)] plus $\mathcal{H}_Z^\parallel$ or $\mathcal{H}_Z^\perp$ to simulate the magnetization and specific heat down to low temperatures, using the integrable Bethe ansatz method (only available for $H \parallel z$ and $N \to \infty$) [51–54] and 100-site ($N = 100$) SSE quantum Monte Carlo algorithm [55,56].

D. Perturbations beyond the nearest neighbors

Our semiquantitative DFT + U simulations [38] suggest that the NNN intrachain coupling is weakly antiferromagnetic in $LuCu(OH)_3SO_4$, $J_2/J_1 \sim 1\%$. The antiferromagnetic J_2 induces spin frustration and the notorious sign problem, generally impeding exact resolutions. Fortunately, J_2/J_1 in $LuCu(OH)_3SO_4$ is significantly smaller, $\sim$1%, compared to the critical value $J_2^c/J_1 = 25\%$ reported in the theoretical works [11,12]. Furthermore, our many-body simulations confirm the negligible effects of the NNN intrachain coupling ($J_2 = 1\%J_1$) on both magnetization and specific heat [38]. Hence, we can safely disregard the J_2 terms in the effective XXZ Hamiltonian of Eq. (3).

Conversely, the minor interchain couplings can trigger a magnetic transition and notably influence observations at low temperatures. Despite the strong ferromagnetic intrachain coupling, the presence of weak but non-negligible interchain couplings induces a three-dimensional (3D) antiferromagnetic order below $T_c = 2.5$ K (see below), akin to observations in Li_2CuO_2 [24] and $Ca_2Y_2Cu_5O_2$ [27]. For simplicity, we address these small interchain couplings at a mean-field level for $H^\perp > H_c^\perp$ [see Fig. 3(a)],

$$\widetilde{\mathcal{H}^\perp} = -\sqrt{J_1^2+D^2}\sum_j \left(S_j^x S_{j+1}^x + S_j^y S_{j+1}^y + \Delta S_j^z S_{j+1}^z\right) - (\mu_0 H^\perp g^\perp - 6J_p\langle S^x\rangle)\sum_j S_j^x, \tag{4}$$

where $J_p = J_{1p}/3 + 2J_{2p}/3$. After a sufficient number of self-consistent iterations ($\geqslant 200$), we obtain the transverse magnetization $M_{calc}^\perp = g^\perp\langle S^x\rangle = g^\perp\langle\Sigma_j S_j^x\rangle/N$, which is independent of the iteration number. Combined fits to the transverse magnetization ($M^\perp/H^\perp$) measured at $\mu_0 H^\perp =$ 1 and 3 T result in the least standard deviation $\sigma = \sqrt{\Sigma_j (M_{expt,j}^\perp/H_j^\perp - M_{calc,j}^\perp/H_j^\perp)^2/N_d} = 0.0358$ cm^3/mol Cu at $J_p/J_1 = 0.21\%$ [see Fig. 2(d)]. Here, N_d represents the number of experimental data points.

Treating J_{p1} and J_{p2} at the mean-field level reveals two interchain antiferromagnetic orders at low temperatures and magnetic fields: stripe-I order at $J_{p1} > J_{p2}$ and stripe-II order at $J_{p1} < J_{p2}$ (see Fig. 3). Fitting to the critical magnetic field measured at 1.8 K, $\mu_0 H_c^\perp = 0.33(2)$ T, yields two optimal sets of interchain couplings at $J_p/J_1 = 0.21\%$: (I) $J_{p1}/J_1 = 1.01\%$ and $J_{p2}/J_1 = -0.18\%$ and (II) $J_{p1}/J_1 = -0.21\%$ and $J_{p2}/J_1 = 0.42\%$ [Fig. 3(a)]. Both parameter sets agree with the critical temperature T_c measured at $\sim$0 T [see Figs. 3(b) and 3(c)] and well reproduce the magnetization and susceptibility measured on the single-crystal sample at 4.2 K [see Figs. 4(a) and 4(b)]. While we cannot presently distinguish which set of interchain couplings is more applicable for $LuCu(OH)_3SO_4$ based solely on the experimental data, the DFT + U calculations suggest the dominant antiferromagnetic nature of J_{p1}, favoring parameter set I and thus the stripe-I interchain magnetic order.

Our self-consistent mean-field SSE method accurately simulates the experimental data at $T \geqslant 4.2$ K ($> T_c$) or $\mu_0 H^\perp \geqslant 1$ T ($> \mu_0 H_c^\perp$), where the symmetry of the spin system is fully recovered by thermal fluctuations or Zeeman interaction [see Figs. 2(d), 3, 4(a), and 4(b)]. Moreover, the mean-field model also shows excellent agreement with the boundary of $\mu_0 H_c^\perp(T)$ and $T_c(H^\perp)$ in the B-T phase measured on $LuCu(OH)_3SO_4$ [38]. Nevertheless, the calculated magnetic-field-induced transition is considerably sharper than the experimental observations at 1.8 K [see Fig. 4(b)]. Additionally, the mean-field calculations fall short in accurately reproducing the experimental data at low temperatures and magnetic fields (within or near the interchain ordered phase). These discrepancies may stem from neglecting intrachain quantum spin fluctuations in the mean-field treatment of interchain couplings.

In $LuCu(OH)_3SO_4$, the putative interchain antiferromagnetic transition is likely significantly suppressed by the

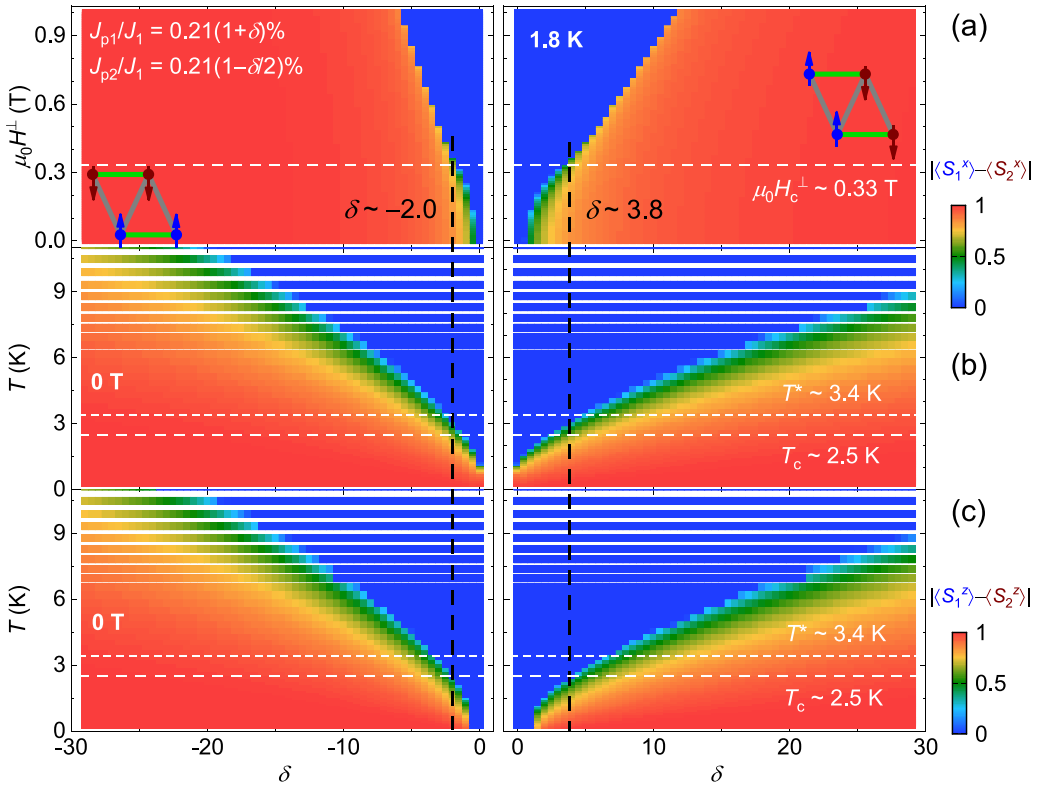

FIG. 3. Interchain antiferromagnetic order parameters calculated using the SSE method with a self-consistent mean-field treatment of interchain interactions. (a) $|\langle S_1^x\rangle - \langle S_2^x\rangle|$ at 1.8 K. (b) $|\langle S_1^x\rangle - \langle S_2^x\rangle|$ at 0 T. (c) $|\langle S_1^z\rangle - \langle S_2^z\rangle|$ at 0 T. The normalized interchain couplings are given as $J_{p1}/J_1 = (1+\delta)J_p/J_1$ and $J_{p2}/J_1 = (-\delta/2)J_p/J_1$, where $J_p/J_1 = 0.21\%$ (antiferromagnetic) is fixed (refer to Fig. 2). At $\delta > 0$, the dominant antiferromagnetic J_{p1} induces interchain stripe-I order along J_{p1} [along green bonds, see right inset of (a)], whereas at $\delta < 0$, the dominant antiferromagnetic J_{p2} causes stripe-II order along J_{p2} [along grey bonds, see left inset of (a)]. The critical field of $\mu_0 H_c^\perp \sim 0.33$ T [dashed white line in (a)] and critical temperature of $T_c \sim 2.5$ K are obtained from the field and temperature dependence of susceptibility measured at $T = 1.8$ K and $H^\perp \to 0$, respectively, on the single-crystal sample (refer to Fig. 4). T^* denotes the temperature at which interchain magnetic ordering starts [see Fig. 4(d)].

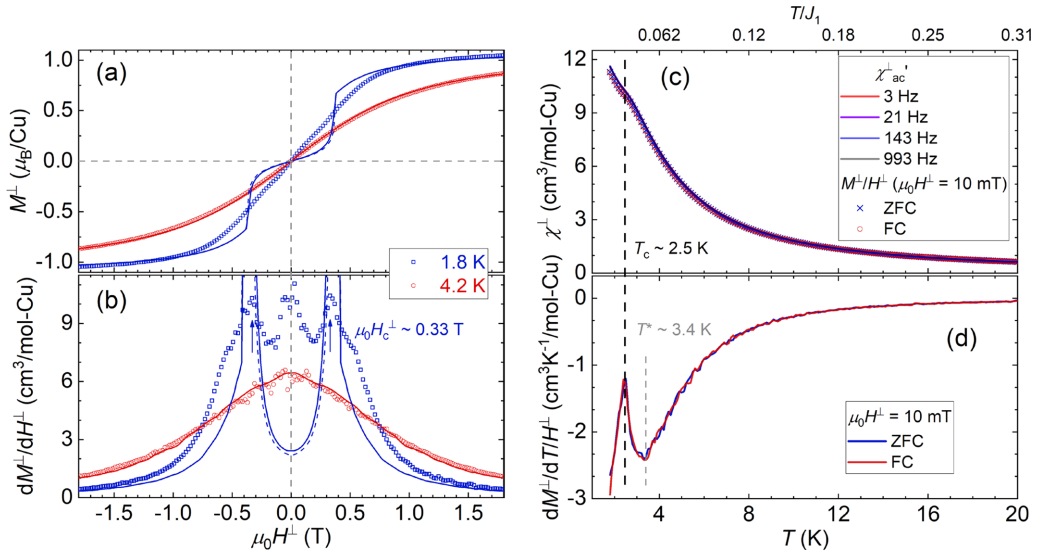

FIG. 4. Magnetization measured on the single-crystal sample. Isothermal (a) magnetization ($M^\perp$) and (b) susceptibilities ($dM^\perp/dH^\perp$) along the b axis. Solid and dashed colored lines represent SSE simulations with the self-consistent mean-field treatment of interchain interactions, using $\delta = 3.8$ and -2.0, respectively; the solid and dashed red lines (at 4.2 K) overlap. The critical field of $\mu_0 H_c^\perp \sim 0.33$ T is indicated by arrows in (b). Although complete loops were measured, no evident magnetic hysteresis was detected. (c) ac susceptibilities measured at various frequencies, and dc susceptibilities measured under zero-field cooling (ZFC) and field cooling (FC). (d) The T-derivative magnetization at $\mu_0 H^\perp = 10$ mT. The critical temperature T_c (~2.5 K) and the onset temperature T^* (~3.4 K) are indicated by dashed lines.

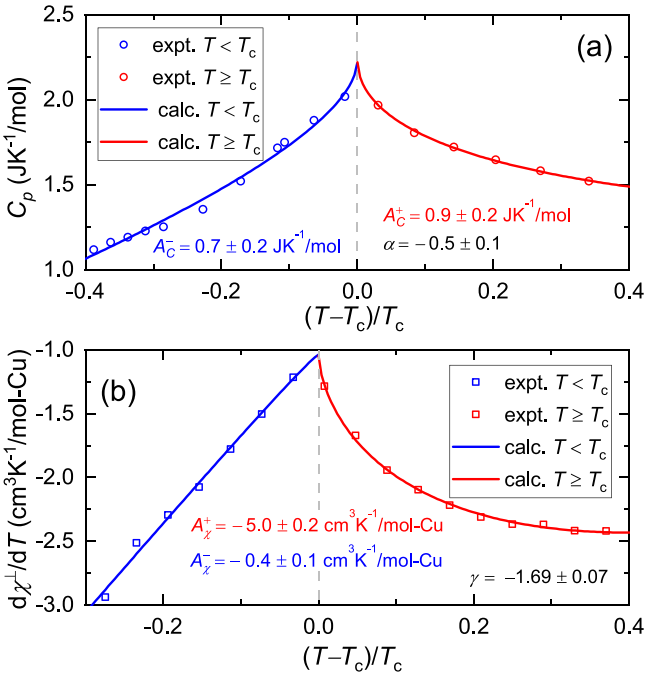

FIG. 5. Temperature dependence of (a) zero-field specific heat (C_p) and (b) T-derivative dc susceptibility ($\mathrm{d}\chi^\perp/\mathrm{d}T = \mathrm{d}M^\perp/\mathrm{d}T/H^\perp$, where $\mu_0 H^\perp = 0.01$ T is applied along the b axis) measured on $LuCu(OH)_3SO_4$. The specific heat data are fitted to $C_p = \frac{A_C^\pm}{\alpha}|t|^{-\alpha} + B_C + E_C t$, whereas the dc susceptibility data are fitted to $\mathrm{d}\chi^\perp/\mathrm{d}T = \mp\gamma A_\chi^\pm |t|^{-\gamma-1} + B_\chi + E_\chi t$, at $T \geqslant T_c$ (+) and $T < T_c$ (−), respectively. Here, $A_C^\pm$ and $A_\chi^\pm$ represent critical-behavior coefficients, the fitted critical exponents α and γ are listed, $B_C + E_C t$ and $B_\chi + E_\chi t$ are caused by noncritical components in a linear-t approximation, $t \equiv (T - T_c)/T_c$, and $T_c = 2.5$ K.

strong quantum spin fluctuations along the chain, as indicated by the weak kinks in susceptibility [$\mathrm{d}M^\perp/\mathrm{d}H^\perp$, Fig. 4(b)], magnetization [Figs. 4(c) and 4(d)], and specific heat [Fig. 5(a)] at critical points. The observed peaks in $\mathrm{d}M^\perp/\mathrm{d}H^\perp$ and $\mathrm{d}M^\perp/\mathrm{d}T/H^\perp$ [Figs. 4(b) and 4(d)] suggest that these temperature- and field-induced magnetic transitions are of second order. The absence of frequency dependence in ac susceptibilities, the lack of splitting between ZFC and FC dc susceptibilities [Fig. 4(c)], and the absence of evident magnetic hysteresis in magnetization [Fig. 4(a)] exclude the possibilities of glassy or ferromagnetic nature for these transitions. Finally, as shown in the B-T phase diagram [38], a weak applied field above ∼0.6 T, corresponding to an energy of $\mu_0 H g \mu_B \sim 1\% J_1$, is large enough to overcome the interchain antiferromagnetic correlations driven by $J_{p1}/J_1 = 1.01\%$ and $J_{p2}/J_1 = -0.18\%$ (as discussed above).

Following Refs. [57–59], we conducted traditional Kornblit-Ahlers-Buehler fits to the experimental thermodynamic properties of $LuCu(OH)_3SO_4$ near $T_c = 2.5$ K, as depicted in Fig. 5. However, the fitted critical exponents, $\alpha \sim -0.5$ and $\gamma \sim -1.7$, are significantly smaller than the theoretically predicted values for 3D systems [59]. This discrepancy suggests much broader peaks observed in both C_p and $\mathrm{d}\chi/\mathrm{d}T$ (or χ) of $LuCu(OH)_3SO_4$ at $T_c = 2.5$ K, indicating very unconventional critical behaviors, likely influenced by strong intrachain spin fluctuations. We emphasize that the negative sign of γ is a special novel feature of $LuCu(OH)_3SO_4$, compared to other compounds [59]. This is confirmed by the measured raw susceptibilities, which are (nearly) monotonic functions of temperature, and exhibit only a weak kink at $T_c = 2.5$ K [similar to the specific heat; see Fig. 6(a)], as shown in Fig. 4(c). The measured values of both α and γ can determine the type of the phase transition, which may be useful in future theoretical and experimental investigations.

The weak but nonzero interchain antiferromagnetic couplings could induce a 3D Néel order (see Fig. 3). $LuCu(OH)_3SO_4$ only approximates the pure XXZ chain model, and nonzero interchain couplings are inevitable. As illustrated in Fig. 4(d), $T^* \sim 3.4$ K denotes the higher temperature at which the T-derivative magnetization/susceptibility $\mathrm{d}M/\mathrm{d}T/H$ exhibits anomalies. It approaches the critical temperature $T_c = 2.5$ K, prompting us to define it as the onset temperature of the proposed 3D Néel magnetic order (see Fig. 3).

E. Proximate Tomonaga-Luttinger liquid state

The above observations and simulations suggest that the perturbation interactions beyond the nearest neighbors are weak and only have a marginal effect on the quantum magnetism of $LuCu(OH)_3SO_4$. Since these perturbations are inherent and completely unavoidable in any real materials, we propose $LuCu(OH)_3SO_4$ as the most perfect candidate so far for the ideal spin-1/2 ferromagnetic XXZ chain model [see Eq. (3) with $\mathcal{H}' \sim 0$]. Therefore, below we focus on the direct comparisons between the low-T observations and theoretical expectations of the ideal exactly solvable model (Fig. 6). When the chain length N is less than ∼30, the ED and SSE simulations exhibit evident finite-size effects below ∼8 K (∼$0.1J_1$) despite the periodic boundary condition employed [38], suggesting highly exotic ground-state properties of the spin-1/2 ferromagnetic XXZ chain system with long-distance unconventional entanglements.

It remains technically difficult to measure the single-crystal specific heat and mK magnetization, limited by the crystal size [38]. In the following discussions, we rely on the low-T data measured on the ground powder. $LuCu(OH)_3SO_4$ is suggested to approximate a gapless Tomonaga-Luttinger liquid ground state of the ideal spin-1/2 ferromagnetic XXZ chain model, supported by the following:

(1) Both our experimental data (Figs. 2 and 3) and DFT + U calculations consistently demonstrate $\Delta \sim 0.994$ and $J_2/J_1 \sim 1\%$ ($\ll 1/4$), suggesting $LuCu(OH)_3SO_4$ is deeply inside the Tomonaga-Luttinger-liquid-ground-state region [11,12].

(2) The magnetic entropy measured at 0 T approaches zero at low temperatures (<2 K) from the full value of $R\ln(1 + 2S) = R\ln 2$ at high temperatures (∼100 K), where $S = 1/2$ [see inset of Fig. 6(a)]. This indicates the spin-1/2 (Cu^{2+}) system of $LuCu(OH)_3SO_4$ indeed approaches its ground-state properties below ∼2 K (∼$3\% J_1$).

(3) Below ∼2 K, the magnetic specific heat exhibits a power-law temperature dependence down to the lowest measured temperature [∼0.1 K, see Fig. 6(c)], $C_m \propto T^{0.85}$, at low applied fields of $\leqslant 1$ T ($\mu_0 H g \mu_B \leqslant 2\% J_1$). Moreover, the dc

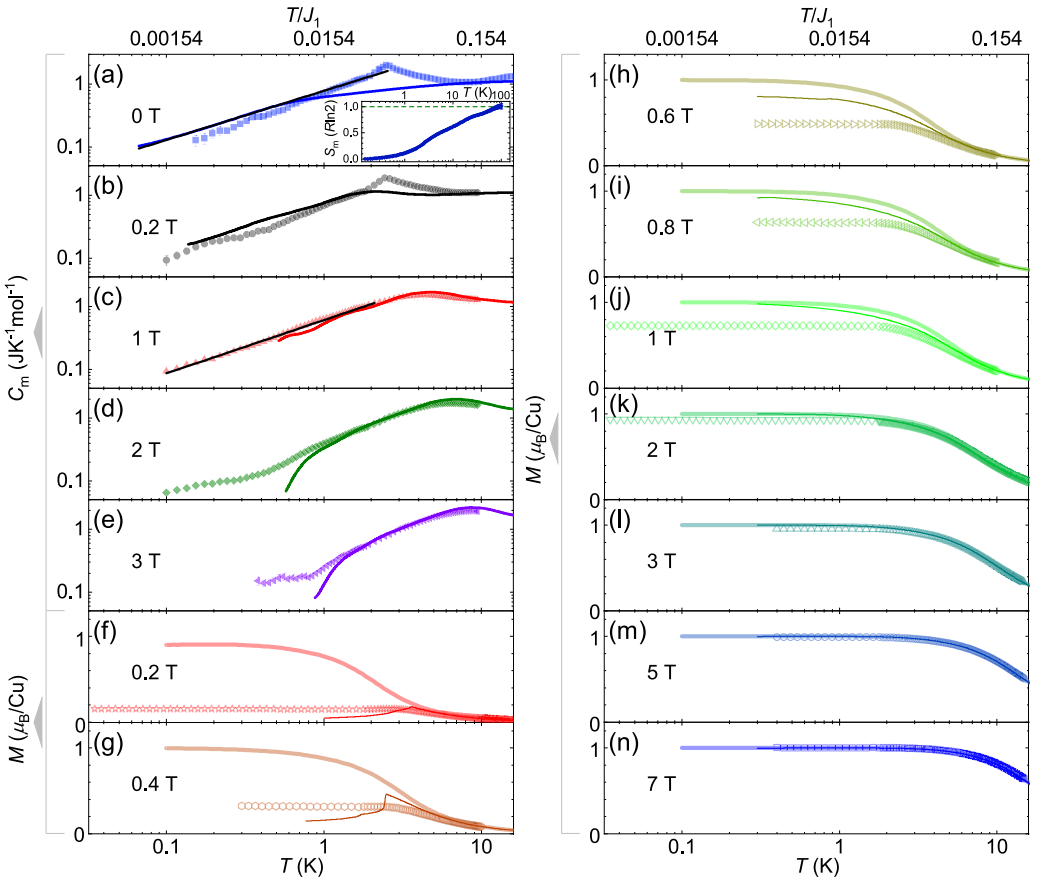

FIG. 6. [(a)–(e)] Low-T magnetic specific heat (C_m) measured on $LuCu(OH)_3SO_4$ powder. The lattice contribution is carefully evaluated and subtracted from the total measured specific heat [38]. The zero-field specific heat is calculated using the Bethe ansatz method [blue line; see (a)], while the non-zero-field data are computed by the SSE method [colored lines; see (b)–(e)]. Here, $J_1 = 65$ K and $\Delta = 0.994$ (ideal XXZ chain model) are used, and the non-zero-field calculations are powder averaged, $C_{m,calc} = 2C^{\perp}_{m,SSE}/3 + C^{\parallel}_{m,Bethe}/3$ [38]. The black line shows a power-law fit to the experimental data measured at 1 T (red triangles) below 2 K in (c), $C_m \propto T^{0.848(7)}$, whereas the black line in (a) displays a power-law fit to the zero-field calculated (Bethe) data between 0.1 and 0.6 K, $C_{m,Bethe}(0\ T) \propto T^{0.782(2)}$. The inset of (a) displays the zero-field magnetic entropy integrated from the experimental data, $S_m(T) = \int_{0.15K}^{T} C_m(T')dT'/T'$. [(f)–(n)] Low-$T$ magnetization measured on $LuCu(OH)_3SO_4$ powder. The thick and thin lines respectively present SSE calculations using the ideal XXZ chain model ($J_1 = 65$ K and $\Delta = 0.994$) and detailed model (with additional $J_{p1}/J_1 = 1.01\%$ and $J_{p2}/J_1 = -0.18\%$) in a powder average. In the detailed model, interchain interactions are treated by a self-consistent mean-field approximation.

magnetization measured at $\mu_0 H = 0.2$ T flattens out to an unsaturated value ($< g/2$) below $\sim$2 K. These observations strongly suggest the gapless nature of the low-lying spin excitations in $LuCu(OH)_3SO_4$.

(4) The ideal spin-1/2 ferromagnetic XXZ chain model ($J_1 = 65$ K and $\Delta = 0.994$) yields the exactly solved specific heat between $\sim$0.1 and 0.6 K, $C_{m,Bethe}(0\ T) \propto T^{0.782(2)}$ [Fig. 6(a)], in good agreement with the experimental findings. The calculated magnetization at 0.2 T also flattens out at low temperatures, qualitatively consistent with the experimental result [Fig. 6(f)].

The applied magnetic field can shift the nuclear Schottky specific heat to higher temperatures [41], possibly contributing to the larger distinctions between the experimental and calculated data at low temperatures in 2 and 3 T [Figs. 6(d) and 6(e)]. Interchain interactions have a minor effect on specific heat, except for the weak peak centered at $T_c \sim 2.5$ K observed at $\mu_0 H < 1$ T. In contrast, interchain interactions (J_{p1} and J_{p2}) significantly suppress magnetization at low temperatures and low applied fields, providing a better explanation for the experimental findings [Figs. 6(f)–6(n)]. Since interchain interactions are treated only at the mean-field level, and a powder average is adopted to lower the computational cost, achieving full quantitative agreement between experimental and simulated magnetization data at low temperatures and applied fields remains extremely challenging. Improved treatment of interchain interactions and larger-size single crystals of $LuCu(OH)_3SO_4$ are highly required for further studies.

IV. CONCLUSIONS

We propose $LuCu(OH)_3SO_4$, a structurally disorder-free compound, as a promising candidate for the exactly solvable spin-1/2 ferromagnetic XXZ chain model ($J_1 = 65$ K and $\Delta = 0.994$). Determined small values for the interchain and NNN intrachain interactions ($J_{p1}/J_1 \sim 1.01\%$, and $J_{p2}/J_1 \sim -0.18\%$, and $J_2/J_1 \sim 1\%$) support this candidacy. Measurements of specific heat and magnetization down to $T = 35$ mK ($\sim 0.0005 J_1$) exhibit gapless ground-state behaviors, aligning

with theoretical expectations for the ideal model. These observations indicate that $LuCu(OH)_3SO_4$ approximates a gapless Tomonaga-Luttinger liquid state at low temperatures. Our findings mark an initial step towards understanding the potential Tomonaga-Luttinger liquid phase in $LuCu(OH)_3SO_4$ and offer new insights for experimental investigations into exactly solvable strongly correlated quantum systems.

ACKNOWLEDGMENTS

We gratefully acknowledge H. Liao for helpful discussion. This work was supported by the National Key R&D Program of China (Grant No. 2023YFA1406500), the National Natural Science Foundation of China (Grant No. 12274153), and the Fundamental Research Funds for the Central Universities (Grant No. HUST: 2020kfyXJJS054).

[1] C. Nayak, S. H. Simon, A. Stern, M. Freedman, and S. Das Sarma, Non-Abelian anyons and topological quantum computation, Rev. Mod. Phys. **80**, 1083 (2008).

[2] S. Yan, D. A. Huse, and S. R. White, Spin-liquid ground state of the $S = 1/2$ kagome Heisenberg antiferromagnet, Science **332**, 1173 (2011).

[3] S. Depenbrock, I. P. McCulloch, and U. Schollwöck, Nature of the spin-liquid ground state of the $S = 1/2$ Heisenberg model on the kagome lattice, Phys. Rev. Lett. **109**, 067201 (2012).

[4] Y. Ran, M. Hermele, P. A. Lee, and X.-G. Wen, Projected-wave-function study of the spin-1/2 Heisenberg model on the kagomé lattice, Phys. Rev. Lett. **98**, 117205 (2007).

[5] H. J. Liao, Z. Y. Xie, J. Chen, Z. Y. Liu, H. D. Xie, R. Z. Huang, B. Normand, and T. Xiang, Gapless spin-liquid ground state in the $S = 1/2$ kagome antiferromagnet, Phys. Rev. Lett. **118**, 137202 (2017).

[6] A. Kitaev, Anyons in an exactly solved model and beyond, Ann. Phys. **321**, 2 (2006).

[7] L. Janssen, E. C. Andrade, and M. Vojta, Magnetization processes of zigzag states on the honeycomb lattice: Identifying spin models for α-$RuCl_3$ and Na_2IrO_3, Phys. Rev. B **96**, 064430 (2017).

[8] J. Wang, B. Normand, and Z.-X. Liu, One proximate Kitaev spin liquid in the $K - J - \Gamma$ model on the honeycomb lattice, Phys. Rev. Lett. **123**, 197201 (2019).

[9] H. Bethe, Zur Theorie der Metalle. I. Eigenwerte und Eigenfunktionen der linearen Atomkette, Z. Phys. **71**, 205 (1931).

[10] W. Heisenberg, *Zur Theorie des Ferromagnetismus* (Springer, Berlin, 1985), Vol. 49, pp. 619–636.

[11] S. Furukawa, M. Sato, and A. Furusaki, Unconventional Néel and dimer orders in a spin-$\frac{1}{2}$ frustrated ferromagnetic chain with easy-plane anisotropy, Phys. Rev. B **81**, 094430 (2010).

[12] S. Furukawa, M. Sato, S. Onoda, and A. Furusaki, Ground-state phase diagram of a spin-$\frac{1}{2}$ frustrated ferromagnetic XXZ chain: Haldane dimer phase and gapped/gapless chiral phases, Phys. Rev. B **86**, 094417 (2012).

[13] M. Enderle, B. Fåk, H.-J. Mikeska, R. K. Kremer, A. Prokofiev, and W. Assmus, Two-spinon and four-spinon continuum in a frustrated ferromagnetic spin-1/2 chain, Phys. Rev. Lett. **104**, 237207 (2010).

[14] S.-L. Drechsler, S. Nishimoto, R. O. Kuzian, J. Málek, W. E. A. Lorenz, J. Richter, J. van den Brink, M. Schmitt, and H. Rosner, Comment on "Two-spinon and four-spinon continuum in a frustrated ferromagnetic spin-1/2 chain", Phys. Rev. Lett. **106**, 219701 (2011).

[15] M. Mourigal, M. Enderle, B. Fåk, R. K. Kremer, J. M. Law, A. Schneidewind, A. Hiess, and A. Prokofiev, Evidence of a bond-nematic phase in $LiCuVO_4$, Phys. Rev. Lett. **109**, 027203 (2012).

[16] K. Nawa, M. Takigawa, M. Yoshida, and K. Yoshimura, Anisotropic spin fluctuations in the quasi one-dimensional frustrated magnet $LiCuVO_4$, J. Phys. Soc. Jpn. **82**, 094709 (2013).

[17] A. Ruff, P. Lunkenheimer, H. K. von Nidda, S. Widmann, A. Prokofiev, L. Svistov, A. Loidl, and S. Krohns, Chirality-driven ferroelectricity in $LiCuVO_4$, npj Quantum Mater. **4**, 24 (2019).

[18] S. E. Dutton, M. Kumar, M. Mourigal, Z. G. Soos, J.-J. Wen, C. L. Broholm, N. H. Andersen, Q. Huang, M. Zbiri, R. Toft-Petersen, and R. J. Cava, Quantum spin liquid in frustrated one-dimensional $LiCuSbO_4$, Phys. Rev. Lett. **108**, 187206 (2012).

[19] H.-J. Grafe, S. Nishimoto, M. Iakovleva, E. Vavilova, L. Spillecke, A. Alfonsov, M.-I. Sturza, S. Wurmehl, H. Nojiri, H. Rosner, J. Richter, U. K. Rößler, S.-L. Drechsler, V. Kataev, and B. Büchner, Signatures of a magnetic field-induced unconventional nematic liquid in the frustrated and anisotropic spin-chain cuprate $LiCuSbO_4$, Sci. Rep. **7**, 6720 (2017).

[20] M. Bosiočić, F. Bert, S. E. Dutton, R. J. Cava, P. J. Baker, M. Požek, and P. Mendels, Possible quadrupolar nematic phase in the frustrated spin chain $LiCuSbO_4$: An NMR investigation, Phys. Rev. B **96**, 224424 (2017).

[21] C. Dussarrat, G. C. Mather, V. Caignaert, B. Domengès, J. G. Fletcher, and A. R. West, Synthesis and crystal structures of Li_2CuZrO_4 polymorphs, J. Solid State Chem. **166**, 311 (2002).

[22] S.-L. Drechsler, O. Volkova, A. N. Vasiliev, N. Tristan, J. Richter, M. Schmitt, H. Rosner, J. Málek, R. Klingeler, A. A. Zvyagin, and B. Büchner, Frustrated cuprate route from antiferromagnetic to ferromagnetic spin-$\frac{1}{2}$ Heisenberg chains: Li_2CuZrO_4 as a missing link near the quantum critical point, Phys. Rev. Lett. **98**, 077202 (2007).

[23] F. Sapiña, J. Rodriguez-Carvajal, M. J. Sanchis, R. Ibanez, A. Beltran, and D. Beltran, Crystal and magnetic structure of Li_2CuO_2, Solid State Commun. **74**, 779 (1990).

[24] W. E. A. Lorenz, R. O. Kuzian, S.-L. Drechsler, W.-D. Stein, N. Wizent, G. Behr, J. Málek, U. Nitzsche, H. Rosner, A. Hiess, W. Schmidt, R. Klingeler, M. Loewenhaupt, and B. Büchner, Highly dispersive spin excitations in the chain cuprate Li_2CuO_2, Europhys. Lett. **88**, 37002 (2009).

[25] R. O. Kuzian, S. Nishimoto, S.-L. Drechsler, J. Málek, S. Johnston, Jeroen van den Brink, M. Schmitt, H. Rosner, M. Matsuda, K. Oka, H. Yamaguchi, and T. Ito, $Ca_2Y_2Cu_5O_{10}$: The first frustrated quasi-1D ferromagnet close to criticality, Phys. Rev. Lett. **109**, 117207 (2012).

[26] J. Thar, R. Müller, S. Mattauch, B. Büchner, and G. A. Roth, Neutron structure investigation of $Ca_2Y_2Cu_5O_{10}$, Acta Crystallogr. A **62**, 185 (2006).

[27] M. Matsuda, J. Ma, V. O. Garlea, T. Ito, H. Yamaguchi, K. Oka, S.-L. Drechsler, R. Yadav, L. Hozoi, H. Rosner, R. Schumann, R. O. Kuzian, and S. Nishimoto, Highly dispersive magnons with spin-gap-like features in the frustrated ferromagnetic

$S = \frac{1}{2}$ chain compound $Ca_2Y_2Cu_5O_{10}$ detected by inelastic neutron scattering, Phys. Rev. B **100**, 104415 (2019).

[28] K. Caslin, R. K. Kremer, F. S. Razavi, A. Schulz, A. Muñoz, F. Pertlik, J. Liu, M.-H. Whangbo, and J. M. Law, Characterization of the spin-$\frac{1}{2}$ linear-chain ferromagnet $CuAs_2O_4$, Phys. Rev. B **89**, 014412 (2014).

[29] B. Willenberg, M. Schäpers, K. C. Rule, S. Süllow, M. Reehuis, H. Ryll, B. Klemke, K. Kiefer, W. Schottenhamel, B. Büchner, B. Ouladdiaf, M. Uhlarz, R. Beyer, J. Wosnitza, and A. U. B. Wolter, Magnetic frustration in a quantum spin chain: The case of linarite $PbCuSO_4(OH)_2$, Phys. Rev. Lett. **108**, 117202 (2012).

[30] L. Heinze, M. D. Le, O. Janson, S. Nishimoto, A. U. B. Wolter, S. Süllow, and K. C. Rule, Low-energy spin excitations of the frustrated ferromagnetic J_1-J_2 chain material linarite $PbCuSO_4(OH)_2$ in applied magnetic fields parallel to the b axis, Phys. Rev. B **106**, 144409 (2022).

[31] W. Wang, Y. Qiao, J. P. Cao, W. M. Liu, and R. H. Liu, Exact ground state and elementary excitations of a competing spin chain with twisted boundary condition, Nucl. Phys. B **975**, 115663 (2022).

[32] Y. Li, D. Adroja, R. I. Bewley, D. Voneshen, A. A. Tsirlin, P. Gegenwart, and Q. Zhang, Crystalline electric-field randomness in the triangular lattice spin-liquid $YbMgGaO_4$, Phys. Rev. Lett. **118**, 107202 (2017).

[33] Y. Li, $YbMgGaO_4$: A triangular-lattice quantum spin liquid candidate, Adv. Quantum Technol. **2**, 1900089 (2019).

[34] Y. Li, S. Bachus, H. Deng, W. Schmidt, H. Thoma, V. Hutanu, Y. Tokiwa, A. A. Tsirlin, and P. Gegenwart, Partial up-up-down order with the continuously distributed order parameter in the triangular antiferromagnet $TmMgGaO_4$, Phys. Rev. X **10**, 011007 (2020).

[35] Y. Li, Q.-Y. Li, W. Li, T. Liu, D. J. Voneshen, P. K. Biswas, and D. Adroja, Spin dynamics and Griffiths singularity in the random quantum Ising magnet $PrTiNbO_6$, npj Quantum Mater. **6**, 34 (2021).

[36] F. Lu, L. Yuan, J. Zhang, B. Li, Y. Luo, and Y. Li, The observation of quantum fluctuations in a kagome Heisenberg antiferromagnet, Commun. Phys. **5**, 272 (2022).

[37] H. J. Lu, K. Diefenbach, Z.-J. Li, H. L. Bao, X. F. Guo, J.-Q. Wang, T. E. Albrecht-Schmitt, and J. Lin, Structural complexity and magnetic orderings in a large family of 3d–4f heterobimetallic sulfates, Inorg. Chem. **59**, 13398 (2020).

[38] See Supplemental Material at http://link.aps.org/supplemental/10.1103/PhysRevMaterials.8.074410 for detailed information about experimental and numerical procedures, which includes Refs. [60–64].

[39] Y. Shimizu, Y. Kono, T. Sugiyama, S. Kittaka, Y. Shimura, A. Miyake, D. Aoki, and T. Sakakibara, Development of high-resolution capacitive Faraday magnetometers for sub-Kelvin region, Rev. Sci. Instrum. **92**, 123908 (2021).

[40] Y. Li, S. Bachus, B. Liu, I. Radelytskyi, A. Bertin, A. Schneidewind, Y. Tokiwa, A. A. Tsirlin, and P. Gegenwart, Rearrangement of uncorrelated valence bonds evidenced by low-energy spin excitations in $YbMgGaO_4$, Phys. Rev. Lett. **122**, 137201 (2019).

[41] Y. Li, S. Bachus, Y. Tokiwa, A. A. Tsirlin, and P. Gegenwart, Gapped ground state in the zigzag pseudospin-1/2 quantum antiferromagnetic chain compound $PrTiNbO_6$, Phys. Rev. B **97**, 184434 (2018).

[42] J. Liu, L. Yuan, X. Li, B. Li, K. Zhao, H. Liao, and Y. Li, Gapless spin liquid behavior in a kagome Heisenberg antiferromagnet with randomly distributed hexagons of alternate bonds, Phys. Rev. B **105**, 024418 (2022).

[43] T. Moriya, Anisotropic superexchange interaction and weak ferromagnetism, Phys. Rev. **120**, 91 (1960).

[44] A. Zorko, S. Nellutla, J. van Tol, L. C. Brunel, F. Bert, F. Duc, J.-C. Trombe, M. A. de Vries, A. Harrison, and P. Mendels, Dzyaloshinsky-Moriya anisotropy in the spin-1/2 kagome compound $ZnCu_3(OH)_6Cl_2$, Phys. Rev. Lett. **101**, 026405 (2008).

[45] In $LuCu(OH)_3SO_4$, each unit cell contains two spins along each chain.

[46] Y. Li, G. Chen, W. Tong, L. Pi, J. Liu, Z. Yang, X. Wang, and Q. Zhang, Rare-earth triangular lattice spin liquid: A single-crystal study of $YbMgGaO_4$, Phys. Rev. Lett. **115**, 167203 (2015).

[47] A. C. Saladino and S. C. Larsen, Relativistic DFT calculations of copper hyperfine coupling constants: Effect of spin-orbit coupling, J. Phys. Chem. A **107**, 5583 (2003).

[48] J. Liu, B. Liu, L. Yuan, B. Li, L. Xie, X. Chen, H. Zhang, D. Xu, W. Tong, J. Wang, and Y. Li, Frustrated magnetism of the triangular-lattice antiferromagnets α-CrOOH and α-CrOOD, New J. Phys. **23**, 033040 (2021).

[49] T. G. Castner and M. S. Seehra, Antisymmetric exchange and exchange-narrowed electron-paramagnetic-resonance linewidths, Phys. Rev. B **4**, 38 (1971).

[50] D. N. Aristov and S. V. Maleyev, Spin chirality induced by the Dzyaloshinskii-Moriya interaction and polarized neutron scattering, Phys. Rev. B **62**, R751 (2000).

[51] M. Takahashi and M. Yamada, Spin-1/2 one-dimensional Heisenberg ferromagnet at low-temperature, J. Phys. Soc. Jpn. **54**, 2808 (1985).

[52] P. Schlottmann, Critical behavior of the isotropic ferromagnetic quantum Heisenberg chain, Phys. Rev. Lett. **54**, 2131 (1985).

[53] M. Takahashi, Simplification of thermodynamic Bethe-ansatz equations, in *Physics and Combinatrics*, edited by A. K. Kirillov and N. Liskova (World Scientific, Singapore, 2001), pp. 299–304.

[54] M. Takahashi, Thermodynamics and correlation functions of XXZ chain, Czech. J. Phys. **53**, 1125 (2003).

[55] O. F. Syljuåsen and A. W. Sandvik, Quantum Monte Carlo with directed loops, Phys. Rev. E **66**, 046701 (2002).

[56] A. W. Sandvik, Stochastic series expansion method with operator-loop update, Phys. Rev. B **59**, R14157 (1999).

[57] A. Kornblit, G. Ahlers, and E. Buehler, Heat capacity of $RbMnF_3$ and EuO near the magnetic phase transitions, Phys. Lett. A **43**, 531 (1973).

[58] A. Kornblit and G. Ahlers, Heat capacity of EuO near the Curie temperature, Phys. Rev. B **11**, 2678 (1975).

[59] J. Wosnitza, From thermodynamically driven phase transitions to quantum critical phenomena, J. Low Temp. Phys. **147**, 249 (2007).

[60] Y. Wang, S. Lany, J. Ghanbaja, Y. Fagot-Revurat, Y. P. Chen, F. Soldera, D. Horwat, F. Mücklich, and J. F. Pierson, Electronic structures of Cu_2O, Cu_4O_3, and CuO: A joint experimental and theoretical study, Phys. Rev. B **94**, 245418 (2016).

[61] G. Kresse and J. Furthmüller, Efficiency of *ab-initio* total energy calculations for metals and semiconductors using a plane-wave basis set, Comput. Mater. Sci. **6**, 15 (1996).

[62] G. Kresse and J. Furthmüller, Efficient iterative schemes for *ab initio* total-energy calculations using a plane-wave basis set, Phys. Rev. B **54**, 11169 (1996).

[63] J. P. Perdew, K. Burke, and M. Ernzerhof, Generalized gradient approximation made simple, Phys. Rev. Lett. **77**, 3865 (1996).

[64] A. W. Sandvik, Computational studies of quantum spin systems, AIP Conf. Proc. **1297**, 135 (2010).